

# H<sub>2</sub> Activation with Co Nanoparticles Encapsulated in N-Doped Carbon Nanotubes for Green Synthesis of Benzimidazoles

Chuncheng Lin,<sup>[a]</sup> Weihao Wan,<sup>[a]</sup> Xueting Wei,<sup>[a]</sup> and Jinzhu Chen<sup>\*[a]</sup>

Co nanoparticles (NPs) encapsulated in N-doped carbon nanotubes (Co@NC<sub>900</sub>) are systematically investigated as a potential alternative to precious Pt-group catalysts for hydrogenative heterocyclization reactions. Co@NC<sub>900</sub> can efficiently catalyze hydrogenative coupling of 2-nitroaniline to benzaldehyde for synthesis of 2-phenyl-1*H*-benzo[*d*]imidazole with >99% yield at ambient temperature in one step. The robust Co@NC<sub>900</sub> catalyst can be easily recovered by an external magnetic field after the reaction and readily recycled for at least six times without any evident decrease in activity. Kinetic experiments indicate that

Co@NC<sub>900</sub>-promoted hydrogenation is the rate-determining step with a total apparent activation energy of 41 ± 1 kJ mol<sup>-1</sup>. Theoretical investigations further reveal that Co@NC<sub>900</sub> can activate both H<sub>2</sub> and the nitro group of 2-nitroaniline. The observed energy barrier for H<sub>2</sub> dissociation is only 2.70 eV in the rate-determining step, owing to the presence of confined Co NPs in Co@NC<sub>900</sub>. Potential industrial application of the earth-abundant and non-noble transition metal catalysts is also explored for green and efficient synthesis of heterocyclic compounds.

## Introduction

Efforts to explore earth-abundant and non-noble transition metal catalysts have always been going on in industry in order to bring an efficient catalytic process into real applications.<sup>[1–3]</sup> Recently, non-precious transition-metal-based catalysts, involving Fe, Co and Ni, were developed by encapsulating into nitrogen-doped or nitrogen-containing carbon frameworks to improve their stability and durability.<sup>[4–6]</sup> These encapsulated catalysts have received a growing attention as potential alternatives to precious Pt-group cathodes in various electrochemical reactions such as CO<sub>2</sub> reduction, water splitting, oxygen reduction and hydrogen evolution.<sup>[5,7–12]</sup> These confined electro-catalysts demonstrate high activity, small overpotential and long-term durability in strong acidic or basic electrolytes and exhibit quite close electro-catalytic performance to commercially available Pt/C catalyst.<sup>[9,13]</sup> Evidently, these embedded catalysts are typically identified by their stability and durability with high tolerance to reaction medium when compared with surface-supported catalysts by traditional preparation method.<sup>[14–17]</sup>

Notably, in sharp contrast, research on thermally induced redox transformations is very limited by using these encapsulated transition metal catalysts. In the cases of reductive reactions, for instance, encapsulated Fe, Co, Ni and bimetallic FeCo, NiCo nano-catalysts were reported for hydrogenation and

transfer hydrogenation of nitroarenes.<sup>[18–24]</sup> A synergistic effect between the embedded transition metal NPs and the surrounded N-doped carbon was suggested for the observed catalytic performance of these encapsulated catalyst.<sup>[25–30]</sup> Confined Co was investigated for hydrogenation of quinoline and biomass-based aldehyde, ketone, and carboxyl, as well as transfer hydrogenation of N-heterocycles.<sup>[22,24,31,32]</sup> Finally, embedded bimetallic NiCo was examined with selective hydrogenation of alkenes and alkynes.<sup>[23]</sup> In contrast, oxidative reactions mainly focus on encapsulated Co catalysts for oxidative dehydrogenation of N-heterocycles, aerobic oxidation of alcohols, hydrocarbons, and *p*-cresols.<sup>[33–35]</sup>

Generally, the encapsulated structure effectively enhances catalyst stability by protecting the confined metal-NPs within the carbon shells from leaching, aggregation, poisoning and harsh/corrosive reaction conditions. For example, an acid-resistant catalyst of carbon nitride (CN) with underlying Ni was investigated for nitroarene hydrogenation under strongly acidic conditions.<sup>[36]</sup> In this nanocomposite catalyst, the inert outer layer of CN protects active Ni from acid-corrosion; while, the inner metallic Ni core activates the inert CN for hydrogenation. Additionally, theoretical research on these encapsulated catalysts demonstrates electron transfer from the confined metal to the nearby carbon shells, which thereby redistributes electron density, increases the density of state (DOS) near Fermi level, lowers the local work function, promotes formation of active sites, and reduces adsorption free energy of the reaction substrate on the outer carbon surface.<sup>[1,37,38]</sup> Inspired by the above results, a robust encapsulated catalyst was thus designed in this research for syntheses of benzimidazole compounds with widely pharmaceutical, medicinal and industrial interests.

As typically important bioactive heterocyclic compounds, benzimidazoles have been extensively investigated for their broad spectrum in biological and pharmacological activities in

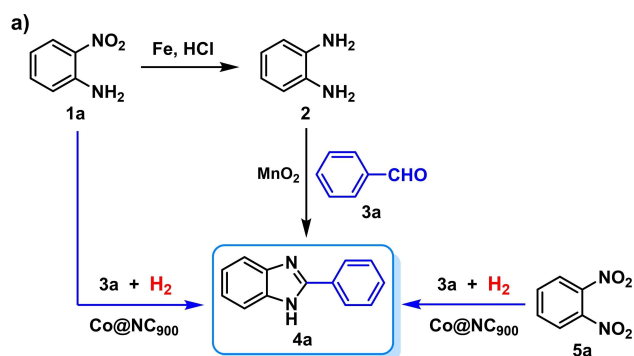
[a] C. Lin, W. Wan, X. Wei, Prof. J. Chen  
Department of Chemistry, College of Chemistry and Materials Science  
Jinan University, No. 855, East Xingye Avenue, Panyu District, Guangzhou  
511443 (P. R. China)

E-mail: chenjz@jnu.edu.cn

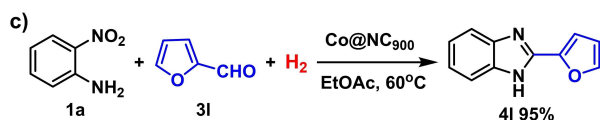
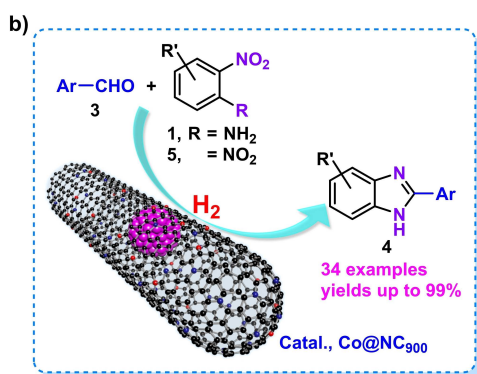
Supporting information for this article is available on the WWW under  
<https://doi.org/10.1002/cssc.202002344>

antibacterial, antifungal, antiviral, anti-inflammatory, anti-ulcer, antihypertensive, antihistamine, antitumor, anticancer, and anti-HIV.<sup>[39–44]</sup> Therefore, various synthetic methods were developed.<sup>[45–48]</sup> However, these synthetic processes generally suffer from various limitations such as the use of strong acidic reaction medium, toxic solvents, high reaction temperature, reactive reagent, strong dehydrating agent, oxidizing agent, and noble metal catalysts.<sup>[49–54]</sup> For example, the most traditional method for 2-phenyl-1*H*-benzo[*d*]imidazole (**4a**) synthesis involves condensation of 1,2-phenylenediamine (**2**) with benzaldehyde (**3a**, Scheme 1a),<sup>[55]</sup> whereas **2** is industrially obtained by 2-nitroaniline (**1a**) reduction.<sup>[56]</sup> Therefore, a directly hydrogenative coupling between **1a** and **3a** in one-step is a very promising and green route for **4a** synthesis by using transition metal catalysts.

Herein, we report that Co NPs encapsulated in N-doped carbon nanotubes (Co@NC<sub>900</sub>), as a robust and magnetic catalyst, can efficiently promote hydrogenative coupling of **1a** [or 1,2-dinitrobenzene (**5a**)] to **3a** for **4a** synthesis with the yield exceeding 99% at room temperature (Scheme 1a). Additionally, Co@NC<sub>900</sub> can readily catalyze reductive heterocyclization of a wide range of substrates **1** or **5** to various aldehydes **3** for synthesis of up to 34 different benzimidazoles (Scheme 1b).



*this work: 4a yield >99%, non-noble metal catal., one step, room temp.*



**Scheme 1.** a) Synthetic route to **4a**. b) Co@NC<sub>900</sub>-promoted hydrogenative coupling of **1** or **5** with **3** for the synthesis of **4**. c) Synthesis of **4l**.

As an important and efficient application of this method, commercially available fuberidazole (**4l**, Scheme 1c), a seed-dressing agent against fusarium disease,<sup>[57–59]</sup> was quantitatively obtained by Co@NC<sub>900</sub> in one step under mild reaction conditions.

## Results and Discussion

In this research, the sample of Co NPs encapsulated in N-doped carbon nanotubes (denoted as Co@NC<sub>T</sub>) was obtained by a multi-step pyrolysis a mixture of triblock copolymer P123, melamine and cobalt acetate at various temperature under N<sub>2</sub> atmosphere, followed by a thoroughly leaching with 1 M HCl at 80 °C for 12 h (see the Supporting Information, Figure S1). The resulting magnetic Co@NC<sub>T</sub> sample was further examined with inductively coupled plasma-atomic emission spectroscopy (ICP-AES) until no soluble Co ions was observed before the subsequent characterization and catalytic reaction. The subscript T in Co@NC<sub>T</sub> indicates the final pyrolysis temperature for Co@NC<sub>T</sub> formation. For instance, Co@NC<sub>900</sub> is obtained by pyrolysis a mixture of P123, melamine and cobalt acetate at 900 °C. For comparison purpose, N-doped carbon (NC<sub>900</sub>) was prepared with similar synthetic procedure as Co@NC<sub>900</sub> without addition of cobalt acetate. To probe the effect of the confined Co NPs on the catalytic performance of Co@NC<sub>900</sub>, Co catalysts supported on the surface of Co@NC<sub>900</sub> (Co/Co@NC<sub>900</sub>) and NC<sub>900</sub> (Co/NC<sub>900</sub>) were also investigated in this research.

The microstructures of Co@NC<sub>900</sub> was initially analyzed by Scanning Electron Microscopy (SEM) and transmission electron microscopy (TEM). The SEM image of Co@NC<sub>900</sub> exhibits a regular and tubular morphology (Figure S3a,b). According to the TEM images, Co@NC<sub>900</sub> adopts a typical architecture of bamboo-like carbon nanotubes with diameter ranging from 30–50 nm (Figure 1a,b). Moreover, the cobalt NPs, with the diameter range of 15–25 nm, are encapsulated at the tip or in the middle of the nanotubes. The high resolution TEM of Co@NC<sub>900</sub> further confirms that the Co NPs are confined by thin layers of graphitic carbon with the carbon-wall thickness around 1–2 nm (Figure 1c).

The Co@NC<sub>900</sub> inner core exhibits (200) lattice fringes with an interspacing of 0.17 nm, which is in accordance with the Co crystal structure, whereas the outer carbon-shell shows graphite (002) fringes with an interspacing of 0.34 nm. Moreover, TEM Energy-Dispersive X-ray Spectrometry (EDX) confirms the presence of C, N and Co elements in Co@NC<sub>900</sub>. The Co core of Co@NC<sub>900</sub> is encapsulated by an N-doped carbon layer, as shown by EDX elemental mapping (Figure 1i–l). The TEM images of both Co@NC<sub>800</sub> (Figure 1d,e) and Co@NC<sub>700</sub> (Figure 1f,g) show irregular and porous sponge-like structure with confined Co NPs as cores of graphitic carbon. The lattice fringes of Co crystal and graphite in both Co@NC<sub>800</sub> and Co@NC<sub>700</sub> are similar with those of Co@NC<sub>900</sub> sample. The formation of porosity in both Co@NC<sub>800</sub> and Co@NC<sub>700</sub> is attributed to HCl leaching with incompletely coated Co NPs as porogens. Evidently, pyrolysis temperature plays a key role on the architecture of the resulting Co@NC<sub>T</sub> series samples. The TEM

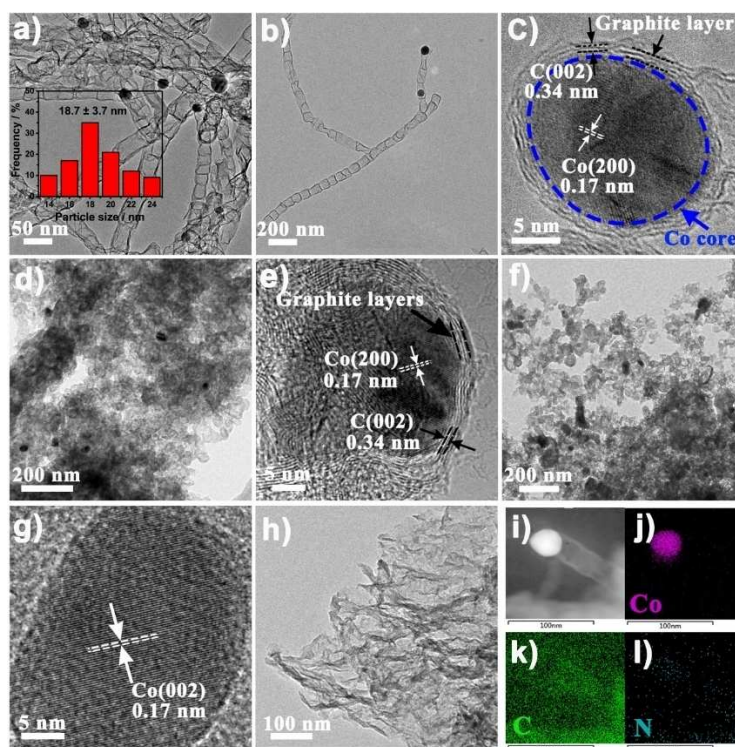


**Figure 1.** TEM images: a–c) Co@NC<sub>900</sub>; d,e) Co@NC<sub>800</sub>; f,g) Co@NC<sub>700</sub>; h) NC<sub>900</sub>. i–l) TEM-EDX of Co@NC<sub>900</sub>.

image of NC<sub>900</sub> exhibits thin-layer nanosheet structure (Figure 1h), demonstrating the promotion effect of Co NPs on the formation of nanotube morphology. The TEM images of Co/NC<sub>900</sub> show supported Co NPs on the thin layers carbon-nanosheet of NC<sub>900</sub> support (Figure S3c,d). Similarly, TEM analysis of Co/Co@NC<sub>900</sub> confirms the loading of Co NPs on the out surface of tubular Co@NC<sub>900</sub> support (Figure S3e,f).

The N<sub>2</sub> sorption isotherm of Co@NC<sub>900</sub> shows a type-IV isotherm with a specific Brunauer-Emmet-Teller (BET) surface area of 648 m<sup>2</sup>g<sup>-1</sup> and an average pore diameter of 3.5 nm (Figure 2a,b and Table 1). The evident hysteresis loop in a wide range from 0.4 to 1.0 *P/P*<sub>0</sub> further confirms the existence of mesoporous structure. In contrast to the tubular morphology of Co@NC<sub>900</sub>, Co@NC<sub>800</sub> has a porous sponge-like structure, thus

yielding an increased specific BET surface area to 708 m<sup>2</sup>g<sup>-1</sup> (Table 1). Co@NC<sub>700</sub> exhibits a decreased specific BET surface area to 541 m<sup>2</sup>g<sup>-1</sup> (Table 1). Generally, all Co@NC<sub>T</sub> serial samples displayed a mesopore-dominated structure with a mean pore diameter of 3.5–3.9 nm, demonstrating a porogen function of the unconfined Co NPs. NC<sub>900</sub> has a specific BET surface area of around 384 m<sup>2</sup>g<sup>-1</sup>, which decreased to 297 m<sup>2</sup>g<sup>-1</sup> upon loading of Co NPs to give Co/NC<sub>900</sub> (Table 1 and Figure S4a,b). Similarly, supporting Co on Co@NC<sub>900</sub> leads to a reduction in surface area to 455 m<sup>2</sup>g<sup>-1</sup> for the Co/Co@NC<sub>900</sub> sample (Table 1 and Figure S4a,b).

The XRD diffraction patterns of Co@NC<sub>900</sub> display one weak peak at 44.2° corresponding to (111) plane of metallic cobalt (Figure 2c), which indicates the presence of metallic cobalt

**Table 1.** Textural parameters of various sample investigated in this research.

Sample	$S_{\text{BET}}^{[a]}$ [m <sup>2</sup> g <sup>-1</sup> ]	$S_{\text{micro}}^{[b]}$ [m <sup>2</sup> g <sup>-1</sup> ]	$S_{\text{meso}}^{[c]}$ [m <sup>2</sup> g <sup>-1</sup> ]	$D_{\text{micro}}/D_{\text{meso}}^{[d]}$ [nm]	$V_{\text{total}}^{[e]}$ [cm <sup>3</sup> g <sup>-1</sup> ]	$V_{\text{micro}}/V_{\text{meso}}^{[f]}$ [cm <sup>3</sup> g <sup>-1</sup> ]
Co@NC <sub>900</sub>	648	74	574	1.0/3.5	1.23	0.04/1.19
Co@NC <sub>800</sub>	708	87	621	-/3.5	1.62	0.12/1.50
Co@NC <sub>700</sub>	541	57	484	1.0/3.9	1.05	0.03/1.02
NC <sub>900</sub>	384	98	285	1.0/3.5	2.00	0.08/1.92
Co/Co@NC <sub>900</sub>	455	110	345	1.0/3.5	1.85	0.03/1.82
Co/NC <sub>900</sub>	297	73	224	1.2/3.7	0.77	-/0.76

[a]  $S_{\text{BET}}$  is the specific surface area calculated by multipoint BET method. [b]  $S_{\text{micro}}$  is the specific surface area of micropores calculated by t-plot method. [c]  $S_{\text{meso}}$  is the surface area of mesopores calculated by  $S_{\text{BET}} - S_{\text{micro}}$ . [d]  $D_{\text{micro}}$  and  $D_{\text{meso}}$  are the micropore and mesopore diameters, respectively, estimated from the local maximum of DFT pore size distribution obtained in the adsorption branch of the N<sub>2</sub> isotherm. [e]  $V_{\text{total}}$  is the total specific pore volume determined by using the adsorption branch of the N<sub>2</sub> isotherm at *P/P*<sub>0</sub> = 0.99. [f]  $V_{\text{micro}}$  is the specific pore volume of micropores determined by the t-plot method and  $V_{\text{meso}}$  is the specific pore volume of mesopores calculated by  $V_{\text{total}} - V_{\text{micro}}$ .

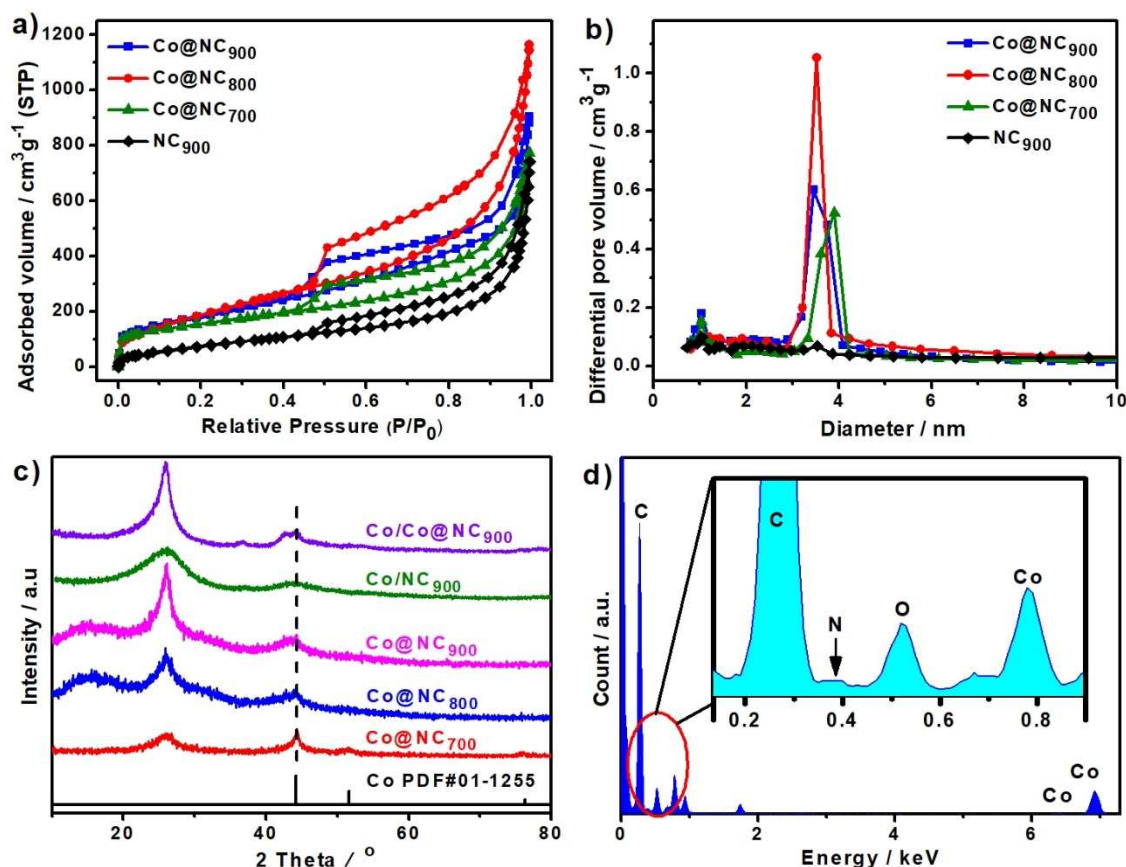


**Figure 2.** a)  $N_2$  adsorption-desorption isotherm of Co@NC<sub>7</sub> serial samples and NC<sub>900</sub>; b) the corresponding pore size distribution. c) XRD patterns of Co/Co@NC<sub>900</sub>, Co/NC<sub>900</sub>, Co@NC<sub>7</sub> serial samples and Co. d) EDX spectra of Co@NC<sub>900</sub>.

species in Co@NC<sub>900</sub>. Moreover, a broad peak at 26.2° for Co@NC<sub>900</sub> is assigned to diffractions from the (002) planes of graphite. Therefore, the XRD analysis conforms a Co@NC<sub>900</sub> structure of encapsulated metallic Co NPs in N-doped carbon nanotubes, which is in line with its TEM analysis (Figure 1a–c). Both Co@NC<sub>800</sub> and Co@NC<sub>700</sub> samples show similar XRD patterns with Co@NC<sub>900</sub> (Figure 2c); however, the graphite diffraction patterns significantly decreased due to a reduced pyrolysis temperature for these two samples. In the cases of Co/Co@NC<sub>900</sub> and Co/NC<sub>900</sub>, two peaks at 26.2° and 44.2° are respectively assigned to the (002) plane of graphite and (111) plane of metallic cobalt (Figure 2c).

Energy-dispersive X-ray spectroscopy (EDX) of Co@NC<sub>900</sub> was then performed to analyze its bulk elemental constituents. The EDX of Co@NC<sub>900</sub> shows a C peak at 0.28 KeV together with an N tail peak (Figure 2d). Moreover, Co@NC<sub>900</sub> exhibits three Co peaks at 0.78 (Co<sub>L<sub>α1</sub></sub>), 6.93 (Co<sub>L<sub>β1</sub></sub>) and 7.65 KeV (Co<sub>L<sub>γ1</sub></sub>).<sup>[38]</sup> The EDX investigation of Co@NC<sub>900</sub> further reveals its composition of C (85.0 wt%), N (1.3 wt%), O (6.6 wt%) and Co (7.1 wt%). A subsequent elemental analysis of Co@NC<sub>900</sub> show its composition of C (83.8 wt%), N (2.2 wt%), O (6.0 wt%) and H (1.9 wt%), which is close to the DEX result. However, due to the effective protection of Co NPs by the N doped carbon layer, our

ICP-AES measurement shows a surface Co content of only 0.14 wt% for Co@NC<sub>900</sub>.

The surface elemental composition and chemical state of Co@NC<sub>900</sub> were determined by X-ray photoelectron spectroscopy (XPS). The survey XPS of Co@NC<sub>900</sub> demonstrates the presence of C (90.9 wt%), N (2.5 wt%), O (5.9 wt%) and Co (0.6 wt%) on the sample surface (Figure 3a and Table S1). In the case of high-resolution Co 2p XPS, the binding energies at 780.6 and 795.4 eV can be assigned to the Co–N<sub>x</sub> moieties, which supports the existence of the coordination between Co and N<sub>x</sub> species (Figure 3b).<sup>[32,60]</sup> Moreover, a nearby peak at 778.8 eV is indexed to the metallic Co species, which is accompanied by two characteristic Co shake-up (satellites) peaks at 785.2 and 802.5 eV.<sup>[61]</sup> The high-resolution N 1s XPS of Co@NC<sub>900</sub> are deconvoluted into four peaks (Figure 3c), corresponding to graphitic-N (401.5 eV), pyrrolic-N (400.9 eV), Co–N (399.7 eV), and pyridinic-N (398.7 eV).<sup>[62,63]</sup> Finally, the C 1s XPS shows four different types of C species which involves C=C (284.8 eV, 53.8%), C–O/C=N (285.5 eV, 17.8%), C–N/C=O (286.6 eV, 15.0%) and O–C=O (290.1 eV, 13.4%), thus indicating the existence of doped heteroatoms such as N and O.<sup>[61,62]</sup>

The 0.6 wt% Co content in Co@NC<sub>900</sub>, observed by XPS analysis, is significantly lower than calculated from EDX (7.1 wt%) due to the sensitivity of XPS analysis to the surface

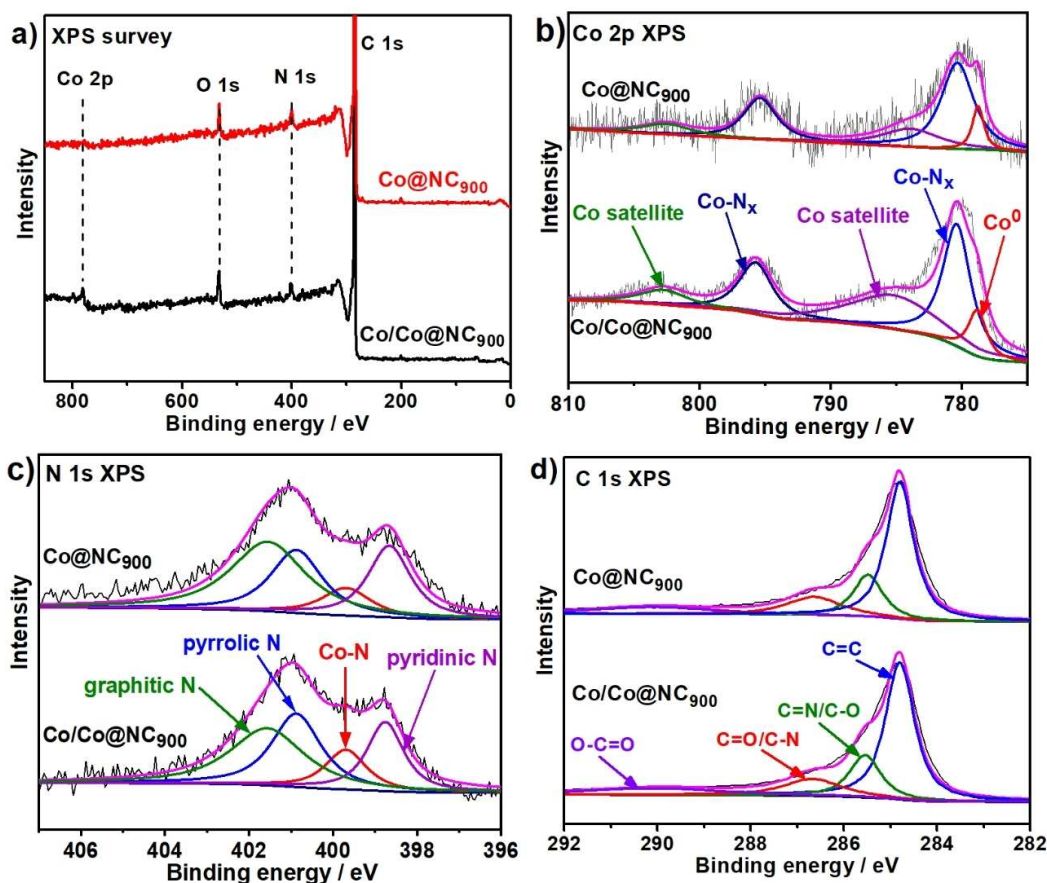


Figure 3. XPS spectra of Co@NC<sub>900</sub> and Co/Co@NC<sub>900</sub>: a) Full survey spectrum; b) Co 2p; c) N 1s; d) C 1s.

chemical composition. Presumably, the Co NPs confined in the graphitic carbon layers of Co@NC<sub>900</sub> can hardly be detected by XPS analysis. However, our thermogravimetric analysis (TGA) indicates Co content of 5.7 wt% based on the assumption that all Co species are transferred into Co<sub>3</sub>O<sub>4</sub> and all C elements are burnt out (Figure S4c).<sup>[64]</sup> Therefore, the Co content of Co@NC<sub>900</sub> determined by EDX is close to TGA result. The above Co content analysis thus demonstrates well protection of graphitic carbon thin layers to the encapsulated Co core in Co@NC<sub>900</sub>. The Co/Co@NC<sub>900</sub> shows almost the same XPS to Co@NC<sub>900</sub> with, however, significantly increased surface Co content (5.7 wt%, Figure 3a,b and Table S1). Moreover, the XPS of Co@NC<sub>800</sub> and Co@NC<sub>700</sub> are very close to that of Co@NC<sub>900</sub> (Table S1 and Figure S5).

The obtained Co@NC<sub>900</sub> was then examined as catalyst for model reaction of **4a** synthesis by reductive heterocyclization of **1a** with **3a** under H<sub>2</sub> atmosphere (Table 2). The blank experiment reveals that **4a** was unobserved without using Co@NC<sub>900</sub> (Table 2, entry 1). Moreover, NC<sub>900</sub> cannot promote the reductive heterocyclization (Table 2, entry 2). In sharp contrast, Co@NC<sub>900</sub> shows remarkable catalytic activity to the reaction by producing quantitative yield of **4a** (Table 2, entry 3). As expected, Co@NC<sub>900</sub> fails to yield **4a** under N<sub>2</sub> atmosphere (Table 2, entry 4). Moreover, the reductive heterocyclization is promoted by an increased loading amount of Co@NC<sub>900</sub>

Table 2. Reductive heterocyclization of **1a** with **3a** for synthesis of **4a** with various catalysts.<sup>[a]</sup>

Entry	Catalyst (mg)	<b>1a</b> conversion [%]	<b>4a</b> yield <sup>[a]</sup> [%]
1	/	/	/
2	NC <sub>900</sub> (10)	/	/
3	Co@NC <sub>900</sub> (20)	> 99	> 99
4 <sup>[b]</sup>	Co@NC <sub>900</sub> (20)	/	/
5	Co@NC <sub>900</sub> (10)	72	71
6	Co@NC <sub>800</sub> (10)	60	57
7	Co@NC <sub>700</sub> (10)	20	18
8	Co/NC <sub>900</sub> (10)	/	/
9	Co/Co@NC <sub>900</sub> (10)	34	32

[a] Reaction conditions: **1a** (0.2 mmol), catalyst (10–20 mg), **3a** (0.4 mmol), H<sub>2</sub> (1.0 MPa), ethyl acetate (EtOAc, 4 mL), RT, 20 h. [b] N<sub>2</sub> (1.0 MPa) was used instead of H<sub>2</sub> (1.0 MPa).

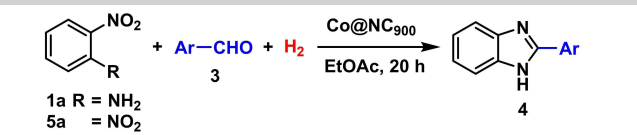
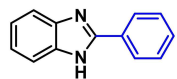
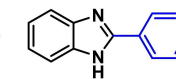
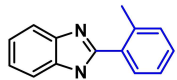
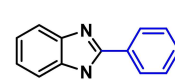
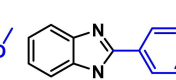
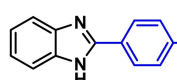
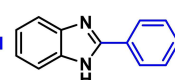
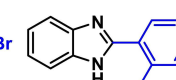
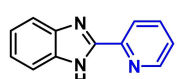
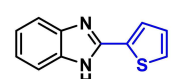
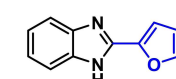
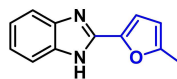
(Table 2, entries 3 and 5), demonstrating an enhanced availability of catalytic active sites for the reaction. The Co@NC<sub>T</sub> serial samples were prepared by pyrolysis a mixture of P123, melamine and cobalt acetate under N<sub>2</sub> atmosphere. Therefore, the correlation between Co@NC<sub>T</sub> activity and its pyrolysis temperature reveals that Co@NC<sub>900</sub>, obtained from 900 °C-

pyrolysis, is the most active among the Co@NC<sub>7</sub> samples (Table 2, entries 5–7).

Previously, Co-based catalysts were reported for hydrogenation reactions.<sup>[65]</sup> Therefore, the presence of Co species in Co@NC<sub>900</sub> could be presumably responsible for the observed activity to H<sub>2</sub> activation. The active species may come from either surface residual Co or encapsulated Co NPs within the NC<sub>900</sub> shell of Co@NC<sub>900</sub>. To address the role of Co on the hydrogenation, the effect of surface residual Co on the reductive heterocyclization was then investigated by experimental methods. Two alternative strategies by catalyst-purification and impurification methods were carried out.<sup>[66]</sup> For purification, Co@NC<sub>900</sub> was further treated with concentrated HCl to remove surface Co species as much as possible. However, the obtained purified Co@NC<sub>900</sub> shows almost the same catalytic activity with its precursor. This result thus demonstrates that the reduced surface-Co species cannot decrease the catalytic activity of Co@NC<sub>900</sub>. In the case of impurification strategy, additional Co was loaded on the surface of Co@NC<sub>900</sub> to give Co/Co@NC<sub>900</sub> with surface Co loading level around 6 wt%. However, the resulting Co/Co@NC<sub>900</sub> exhibits a significantly reduced **4a** yield to 32% when compared with a 71% yield from Co@NC<sub>900</sub> (Table 2, entries 5 and 9). This observation thus reveals that the addition of Co species on the Co@NC<sub>900</sub> surface cannot boost its hydrogenation activity. In addition to Co@NC<sub>900</sub> support, Co was also supported on NC<sub>900</sub> to give a 6 wt% Co/NC<sub>900</sub> sample for comparison purpose. However, the obtained Co/NC<sub>900</sub> shows a negligible activity towards the reductive heterocyclization (Table 2, entries 5 and 8). Therefore, the surface residual Co is thought to inhibit rather than promote the hydrogenation activity of Co@NC<sub>900</sub>. The presence of residual Co species on Co@NC<sub>900</sub> might block true active sites of the catalyst, and thus reduces its catalytic activity. Recent research suggests that a synergetic effect between the embedded transition metal NPs and the surrounded N-atoms is responsible for a heterolytic dissociation of the hydrogen molecule.<sup>[25–30]</sup> This mechanism is more energetically favorable when compared to the homolytic H<sub>2</sub> dissociation process observed for traditional surface-supported NPs catalysts. This phenomenon would also explain the results herein reported, a better performance of Co@NC<sub>900</sub> compared to Co/NC<sub>900</sub>. In conclusion, Co@NC<sub>900</sub> might contain negligible surface Co species; however, the catalytic activity of Co@NC<sub>900</sub> should be in line with its intrinsic activity as proved by the above controlled experiments from purification and impurification strategies. Therefore, the encapsulated Co NPs within the NC<sub>900</sub> shell of Co@NC<sub>900</sub> might actually contribute to the H<sub>2</sub> activation. Its role was subsequently investigated by density functional theory (DFT) calculations (will be discussed below).

Therefore, **4a** yield of >99% with complete **1a** conversion were observed with Co@NC<sub>900</sub> under very mild conditions by using 1.0 MPa H<sub>2</sub> at ambient temperature. Encouraged by the above result, the 2-arylbenzimidazole scope was further investigated by using various aromatic aldehydes **3** with Co@NC<sub>900</sub>. Generally, the method tolerates a wide range of aldehydes for the heterocyclization (Table 3). The substituted benzaldehydes with electron-donating groups, including methyl and methoxy,

**Table 3.** Co@NC<sub>900</sub>-promoted benzimidazole syntheses from **1a/5a** and various aldehydes **3**.<sup>[a]</sup>

		
1a R = NH <sub>2</sub> 5a R = NO <sub>2</sub>		
		
<b>4a</b> 99% <sup>b</sup> (98%)	<b>4b</b> 99% (97%)	<b>4c</b> 97% (94%)
		
<b>4d</b> 99% (97%)	<b>4e</b> 96% (94%)	<b>4f</b> 96% (99%)
		
<b>4g</b> 99% (97%)	<b>4h</b> 68% (69%)	<b>4i</b> 62% (64%) 97% <sup>c</sup> (94%) <sup>c</sup>
		
<b>4j</b> 84% (91%)	<b>4k</b> 98% (98%)	<b>4l</b> 95% (98%)
		
<b>4m</b> 89% <sup>d</sup> (94%) <sup>d</sup>		

[a] Reaction conditions: Co@NC<sub>900</sub> (20 mg), **1a** or **5a** (0.20 mmol), **3** (0.40 mmol), EtOAc (4 mL), H<sub>2</sub> (1.0 MPa), 60 °C for conversion of **1a** and 70 °C for that of **5a**, 20 h. Values in parentheses are yields obtained from **5a**. [b] T = RT. [c] T = 100 °C. [d] T = 130 °C.

produce quantitative yields of the corresponding benzimidazoles (**4b–e**). In the case of halogen-substituted benzaldehydes, both *p*-fluorobenzaldehyde and *p*-chlorobenzaldehyde smoothly undergo the heterocyclization, producing excellent yields of the corresponding benzimidazoles **4f** and **4g**, whereas *p*-bromobenzaldehyde affords moderate yield of 2-(4-bromophenyl)-1*H*-benzo[*d*]imidazole (**4h**). As expected, the heterocyclization of bulky 1-naphthaldehyde also leads to a moderate yield of 2-(1-naphthalenyl)-1*H*-benzo[*d*]imidazole (**4i**), suggesting the presence of steric hindrance effect of the aromatic aldehyde. However, a quantitative **4i** yield up to 97% is observed with the increased reaction temperature. In addition, 2-heteroaromatic-substituted benzimidazoles, bearing 2-pyridyl (**4j**), 2-thienyl (**4k**), or 2-furyl (**4l,m**) substituents, are readily prepared in excellent yields from the corresponding heteroaromatic aldehydes. Transition metal-based homogeneous catalysts were previously reported to undergo deactivation with heteroaromatic compounds containing sulfur atoms (**4k**).<sup>[67]</sup> Notably, both furfural and 5-hydroxymethylfurfural are biomass-based aromatic aldehydes and are applicable to the developed catalytic system (**4l,m**). Moreover, the commercially available

fungicide fuberidazole (**4l**) was obtained in quantitative yields from **1a** and furfural. The above results thus indicate that Co@NC<sub>900</sub> can efficiently promote heterocyclization of **1a** with a

wide range of aromatic aldehydes **3** for various benzimidazole syntheses.

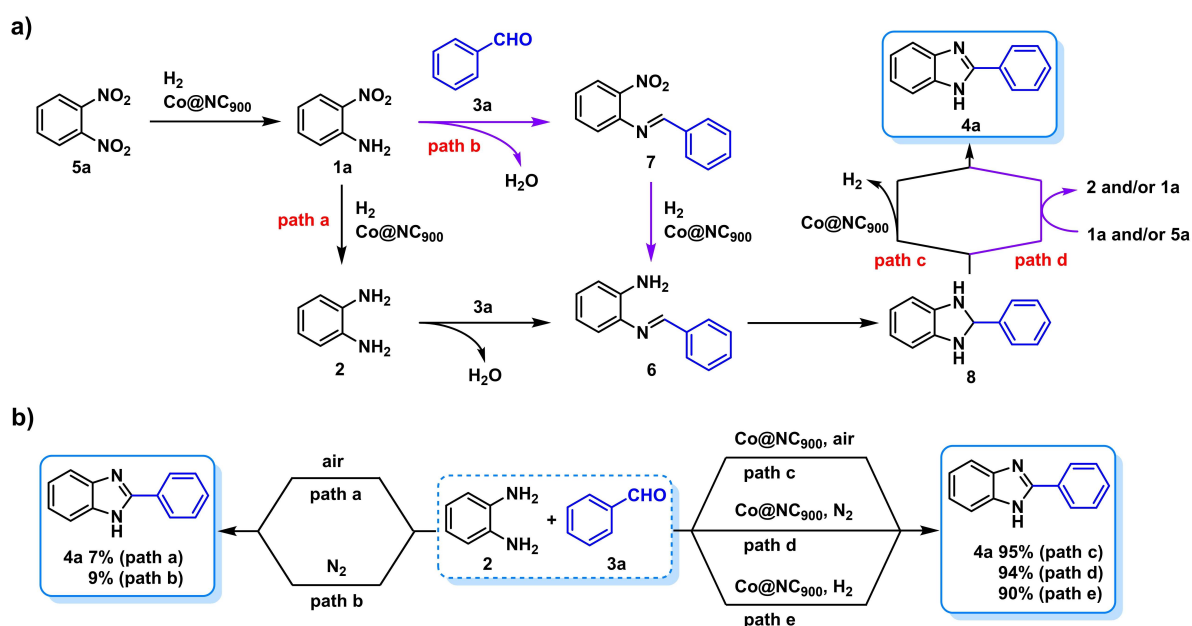
In addition to **1a**, **5a** is smoothly transferred into benzimidazoles **4** in excellent to good yields by Co@NC<sub>900</sub>-promoted reductive heterocyclization with various aldehydes **3** under H<sub>2</sub> atmosphere (Table 3). Under such conditions, Co@NC<sub>900</sub> may initially promote hydrogenation of **5a** to give **1a** as an in situ-formed "intermediate", as a very close yields of **4** are observed with the two precursors of **5a** and **1a** in the heterocyclization reaction (Table 3). Finally, various substituted **1a**, including methyl (**1b–f**), *tert*-butyl (**1g**), methoxy (**1h**) and fluoro groups (**1i**), smoothly undergo the heterocyclization giving excellent yields of **4** (**4n–s**, Table 4), further extending the benzimidazole scope. Notably, steric hindrance effect was observed with *tert*-butyl substituted 2-nitroaniline (**1g**) in the heterocyclization (**4q**, Table 4).

Scheme 2a thus shows a proposed mechanism for transformation of **5a** into **4a** according to our experiments and previous reports. **5a** is initially hydrogenated to **1a** by Co@NC<sub>900</sub>. The subsequent path a (Scheme 2a) demonstrates that successive hydrogenation of **1a** leads to formation of **2**, followed by a condensation of **2** with **3a** to give amino-imine **6**. In contrast, path b (Scheme 2a) shows formation of **6** through preliminary condensation of **1a** with **3a** and a subsequent hydrogenation of nitro-imine **7**. Path a may be a prevailing route due to a higher pK<sub>a</sub> of amino group in **2** than in the case of **1a**, which can facilitate the subsequent condensation process. Intramolecular cyclization of **6** and the following dehydrogenation of **8** yield **4a** with aromatization as a potential driving force. The oxidative dehydrogenation of **8** can be promoted by Co@NC<sub>900</sub> catalyst (Scheme 2a, path c) and/or **1a**/**5a**-oxidation (Scheme 2a, path d).<sup>[23]</sup>

To verify the proposed mechanism, the Co@NC<sub>900</sub>-promoted transformation of **1a** into **4a** was further investigated with

**Table 4.** Synthesis of benzimidazoles from **1** and **3a** using Co@NC<sub>900</sub>.<sup>[a]</sup>

[a] Reaction conditions: Co@NC<sub>900</sub> (20 mg), **1** (0.20 mmol), **3a** (0.40 mmol), EtOAc (4 mL), H<sub>2</sub> (1.0 MPa), 60 °C, 20 h. [b] T = 100 °C.



**Scheme 2.** a) Proposed mechanism and b) controlled experiments for formation of **4a**.

time-dependent gas chromatography-mass spectrometry (GC-MS) analysis. **4a** ( $m/z$  194.1) was detected to increase with reaction time (Figure 4 and Figure S6), suggesting a final product character. Whereas, three species of **2** ( $m/z$  108.1), **6** ( $[6-H]^-$ ,  $m/z$  195.1) and **8** ( $[8-H]^-$ ,  $m/z$  195.1) were observed to be formed initially with very low abundances and later consumed in the interval of time (Figure 4 and Figure S6), thus indicating an intermediate behavior. The above results accordingly suggest path a in Scheme 2a for transformation of **1a** into **4a**. Low intensities of the intermediates **2**, **6**, and **8** demonstrate their fast conversions upon in situ formation without further accumulation (Figure 4). Therefore, hydrogenation of **1a** was presumably the rate-determining step for **4a** formation (Scheme 2a). While, condensation of **2** with **3a**, cyclization of **6**, and dehydrogenation of **8** may smoothly proceed with fast reaction rates under the investigated conditions (Scheme 2a).

Both paths a and b for transformation of **1a** into **6** (Scheme 2a) were further investigated and compared based on reaction kinetics. Path a involves a tandem reaction of hydrogenation of **1a** to **2** and condensation of **2** with **3a** to yield **6**. The kinetics of the hydrogenation of **1a** promoted by Co@NC<sub>900</sub> shows a linear correlation of the initial **1a** hydrogenation rate with Co@NC<sub>900</sub> loading level (Figure 5a) and H<sub>2</sub> pressure (Figure 5b) at various reaction temperatures. Therefore, first-order kinetics of **1a** hydrogenation rate with respect to the Co@NC<sub>900</sub> loading amount and H<sub>2</sub> pressure are respectively suggested based on the proportionately positive influence of catalyst concentration and H<sub>2</sub> pressure on the hydrogenation of **1a**. However, a zero-order kinetic dependence of the initial **1a** hydrogenation rate on **1a** concentration is observed (Figure 5c), suggesting a quick adsorption of **1a** on the Co@NC<sub>900</sub> surface. Generally, the kinetic behaviors of Co@NC<sub>900</sub>-promoted hydrogenation of **1a** are very close to our recently reported nitrobenzene hydrogenation with phosphorus-doped carbon nanotubes as a metal-free catalyst.<sup>[68]</sup> Therefore, a pseudo-first-

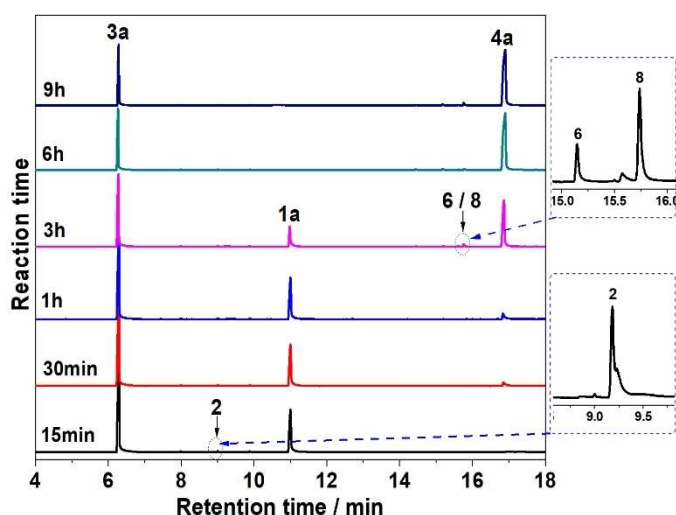


**Figure 4.** Time-dependent GC-MS analysis of **4a** formation. Reaction conditions: Co@NC<sub>900</sub> (10 mg), **1a** (0.2 mmol), **3a** (0.4 mmol), H<sub>2</sub> (1.0 MPa), EtOAc (4.0 mL), 80 °C.

order kinetics is applied to hydrogenation of **1a** with respect to H<sub>2</sub> pressure if considering Co@NC<sub>900</sub> loading level as a constant in the reaction. This assumption is further proven by a linear fitting of  $\ln(1-X)$  vs reaction time (Figure 5d). The resulting Arrhenius plot of  $\ln k_{\text{obs}}$  vs  $(1/T \times 10^3)$  indicates a total apparent  $E_a$  of  $41 \pm 1$  kJ mol<sup>-1</sup> for hydrogenation of **1a** (Figure 5g).

In the case of **2** condensation with **3a**, the reaction follows a second-order kinetics,<sup>[69]</sup> showing proportionally linear dependence of initial condensation rate on both concentrations of **2** and **3a**. A linear kinetic profile of  $1/(1-X)$  vs reaction time further confirms a second-order kinetics of the condensation reaction (Figure 5e). The total apparent  $E_a$  is  $38 \pm 3$  kJ mol<sup>-1</sup> for the condensation of **2** with **3a** based on the Arrhenius equation as shown in Figure 5g. For the condensation of **1a** and **3a** by path b (Scheme 2a), the total apparent  $E_a$  is  $65 \pm 2$  kJ mol<sup>-1</sup> (Figure 5f,g). Therefore, our kinetic experiments reveal total apparent  $E_a$  values of  $41 \pm 1$  kJ mol<sup>-1</sup> for hydrogenation of **1a** and  $38 \pm 3$  kJ mol<sup>-1</sup> for **2**→**3a** condensation in path a, which are all significantly lower than  $65 \pm 2$  kJ mol<sup>-1</sup> for the **1a**→**3a** condensation step in path b. Thus, path a should be a predominant route for the transformation of **1a** into **6** with hydrogenation of **1a** as the rate-determining step.

Finally, control experiments were performed to probe the direct heterocyclization of **2** and **3a** for **4a** formation (Scheme 2b). Treatment **2** with **3a** in the absence of Co@NC<sub>900</sub> leads to quantitative formation of **6** with negligible **4a** yields under N<sub>2</sub> or air atmosphere at ambient temperature (Scheme 2b, paths a and b). In contrast, quantitative **4a** was observed when Co@NC<sub>900</sub> was added into the above reaction systems (Scheme 2b, paths c-e), thus indicating the promotion effect of Co@NC<sub>900</sub> for aromatization of **8** through oxidative dehydrogenation process (Scheme 2a, path c).

Our above controlled experiments thus indicate that **5a**→**4a** transformation follows an initially successive hydrogenation of **5a** to **2** by Co@NC<sub>900</sub> with **1a** as the “intermediate” (Scheme 2a, path a). A subsequent heterocyclization of **2** with **3a** for **4a** formation goes through a tandem reaction of condensation of **2** with **3a**, intramolecular cyclization of **6**, and a final dehydrogenation of **8** by aromatization (Scheme 2a, paths c and d). Co@NC<sub>900</sub>-promoted hydrogenation is the rate-determining step for transformation of **5a** into **4a**, whereas both catalyst Co@NC<sub>900</sub> and weak oxidants such as **1a** and **5a** may accelerate the dehydrogenation process (Scheme 2a, paths c and d).

Finally, the reusability of Co@NC<sub>900</sub> demonstrates that the catalyst was readily recycled for six times at least without loss of its catalytic activity (Figure 5h). Notably, the recovered Co@NC<sub>900</sub> after the recycling shows almost the same morphology with the fresh one, demonstrating the stability of Co@NC<sub>900</sub> (Figure S3g,h).

To probe the effect of encapsulated Co NPs in Co@NC<sub>900</sub> on its catalytic performance, Co<sub>4</sub> cluster encapsulated in a single-walled N-doped carbon nanotube (Co<sub>4</sub>@N-CNT) is designed as a model catalyst of Co@NC<sub>900</sub> for DFT investigation. Although the sizes of the Co<sub>4</sub> cluster and N-CNT considered in the calculation are much smaller and simpler than that of the experimentally observed Co@NC<sub>900</sub>, this reduced geometry can capture the

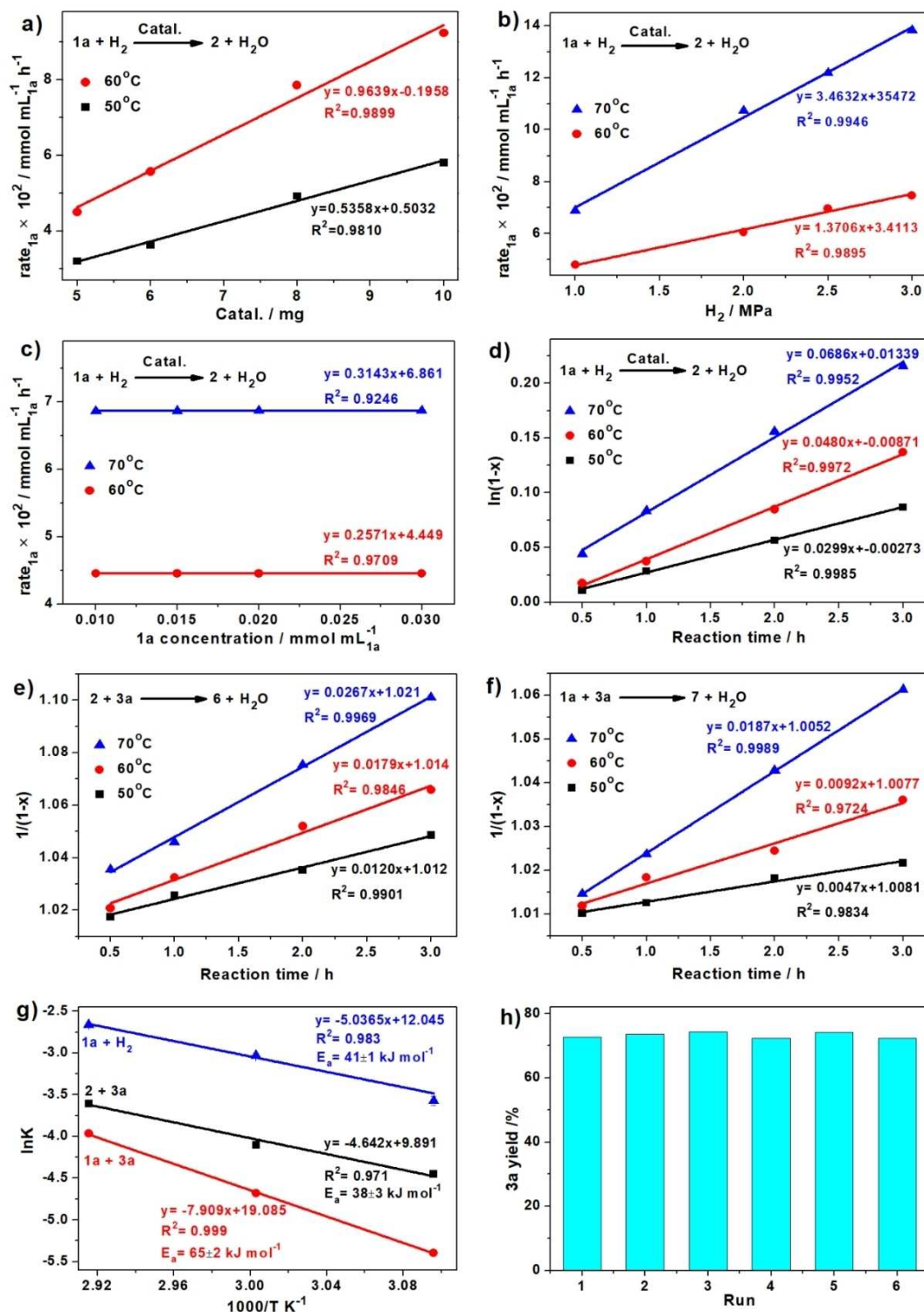


**Figure 5.** a–c) Effects of initial Co@NC<sub>900</sub> loading (a), H<sub>2</sub> pressure (b), and 1a concentration (c) on the initial 1a hydrogenation rate. d) Kinetic plots between ln(1-X) and reaction time for hydrogenation of 1a. e,f) Kinetic profiles between 1/(1-X) and reaction time for 2→3a condensation (e), and 1a→3a condensation (f). g) Arrhenius profiles between observed rate constant  $k_{obs}$  and reaction temperature for 1a hydrogenation, 2→3a condensation, and 1a→3a condensation. h) Reusability of Co@NC<sub>900</sub>. Reaction conditions: a) 1a (0.04 mmol), Co@NC<sub>900</sub> (5–10 mg), EtOAc (4.0 mL), H<sub>2</sub> (1.0 MPa); b) 1a (0.04 mmol), Co@NC<sub>900</sub> (5 mg), EtOAc (4.0 mL), H<sub>2</sub> (1.0–3.0 MPa); c) Co@NC<sub>900</sub> (5 mg), H<sub>2</sub> (1.0 MPa), EtOAc (4.0 mL); d) 1a (0.04 mmol), Co@NC<sub>900</sub> (5 mg), EtOAc (4.0 mL), H<sub>2</sub> (1.0 MPa); e) 3a (0.04 mmol), 2 (0.04 mmol), EtOAc (4.0 mL); f) 3a (0.04 mmol), - 1a (0.04 mmol), EtOAc (4.0 mL); h) Co@NC<sub>900</sub> (10 mg), 1a (0.20 mmol), 3a (0.40 mmol), EtOAc (4.0 mL), H<sub>2</sub> (1.0 MPa), RT, 20 h.

essential character of the electronic structure in  $\text{Co}@NC_{900}$ . Additionally, a single-walled N-doped carbon nanotube (N-CNT) is considered for comparison purpose.

Our control experiments confirmed a key step of  $\text{Co}@NC_{900}$ -promoted hydrogenation of **1a** for the transformation of **1a** into **4a** (Scheme 2a). Therefore, the initial step of hydrogenation of **1a** to 2-nitrosoaniline (**10**) via 2-(dihydroxyamino)aniline (**9**) as intermediate was further investigated over the two model catalysts  $\text{Co}_4@N\text{-CNT}$  and N-CNT for comparison (Figure 6). Figure 6 shows the step-by-step reaction pathway in term of energy diagram based on DFT calculations. The whole hydrogenation process is assumed to proceed through dissociation of  $\text{H}_2$  molecule, adding of hydrogen atom to nitro group of **1a**, and water-removal.

We initially calculated the activation and dissociation of  $\text{H}_2$  molecule on the surface of the two catalyst models (Figure 6).  $\text{H}_2$  is weakly adsorbed on the N-CNT with a negligible adsorption energy of 0.01 eV [N-CNT $\cdot$ ( $\text{H}_2$ ), IM1]. The subsequent H–H bond cleavage on N-CNT is kinetically unfeasible, corresponding to a total endogenic reaction by 2.61 eV [N-CNT $\cdot$ (2H), IM2] with an extremely high energy barrier of 3.54 eV (TS1). In sharp contrast,  $\text{Co}_4@N\text{-CNT}$  exhibits a significantly decreased energy barrier to 2.70 eV (TS1) for the H–H bond dissociation with a corresponding endogenic energy only 1.46 eV [ $\text{Co}_4@N\text{-CNT}\cdot$ (2H), IM2]. These results can be further interpreted in view of orbital overlapping. Figure 7 thus depicts the DOS of H 1s and N 2p in Cat $\cdot$ (2H) state, the overlap between H 1s and N 2p increases in  $\text{Co}_4@N\text{-CNT}\cdot$ (2H) if compared with N-CNT $\cdot$ (2H), indicating a stronger N–H bond within  $\text{Co}_4@N\text{-CNT}\cdot$ (2H) (Figure 6, IM2) than in the case of N-CNT $\cdot$ (2H) (Figure 6, IM2).<sup>[70–72]</sup> In addition, the increased DOS near Fermi level for  $\text{Co}_4@N\text{-$

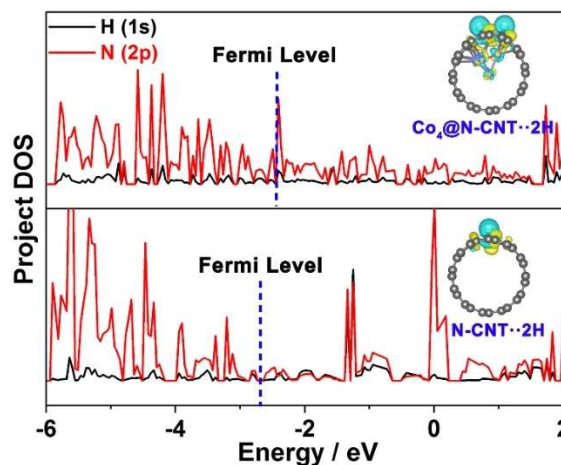


Figure 7. Comparison of projected DOS for H 1s and its bonded N 2p between  $\text{Co}_4@N\text{-CNT}\cdot$ (2H) and N-CNT $\cdot$ (2H). Dashed lines represent the Fermi Level. Yellow and blue regions show charge increase and decrease, respectively.

N-CNT $\cdot$ (2H) is beneficial to its subsequent hydrogenation reaction (Figure 7).<sup>[37]</sup>

After  $\text{H}_2$  dissociation on the catalyst, adsorption of **1a** on the Cat $\cdot$ (2H) adduct is a prerequisite for subsequent hydrogenation of the nitro group. The adsorption energies of **1a** are  $-1.67$  eV on  $\text{Co}_4@N\text{-CNT}\cdot$ (2H) and  $-1.05$  eV on N-CNT $\cdot$ (2H) (IM3), respectively (Figure 6). Subsequent stepwise hydrogenations of **1a** in both adducts of  $\text{Co}_4@N\text{-CNT}\cdot$ (2H) $\cdot$ **1a** and N-CNT $\cdot$ (2H) $\cdot$ **1a** are endothermic from IM3 to IM5 (Figure 6). Nitro group ( $-\text{NO}_2$ ) in Cat $\cdot$ (2H) $\cdot$ **1a** is gradually hydrogenated to form  $-\text{N}(\text{OH})_2$ , thus yielding Cat $\cdot$ **9** adduct. Notably, a successive

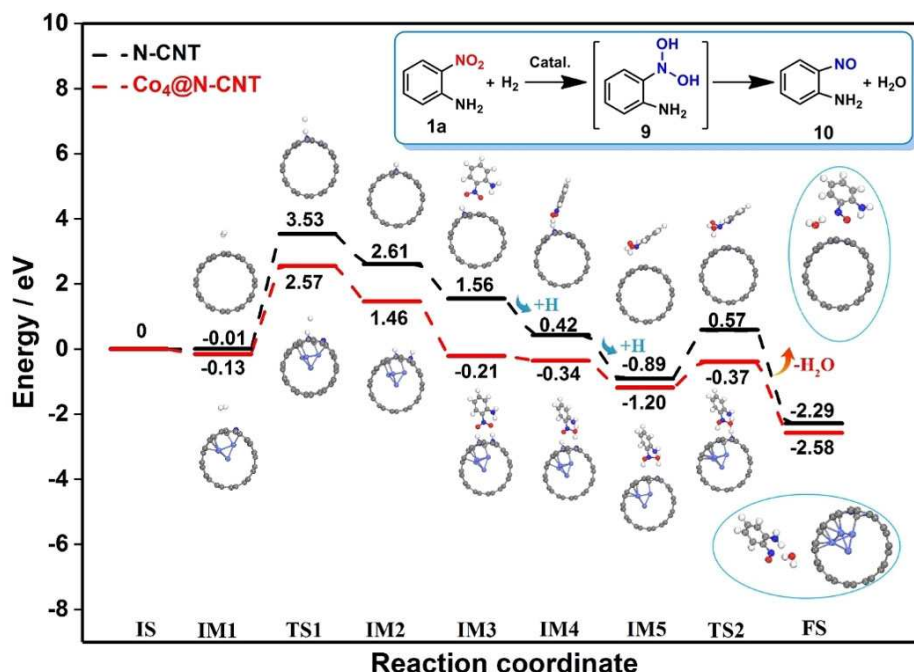


Figure 6. The structures involved in hydrogenation of **1a** to **10** over the two model catalysts. Energies are given in eV.

proton transfer of  $-N(OH)_2$  to form  $-N(O)OH_2$  is observed in N-CNT-9 (from IM5 to TS2) before **9** dehydration (Figure 6 and Figure S7). While, in the case of  $Co_4@N-CNT-9$ , the  $-N(OH)_2$  group forms a hydrogen bond between OH in  $-N(OH)_2$  and N atom on the carbon shell of  $Co_4@N-CNT$  (from IM5 to TS2) before **9** dehydration (Figure 6 and Figure S7).

Finally, the dehydration of Cat-9 adduct shows a lower energy barrier of 0.83 eV for  $Co_4@N-CNT$  than that of N-CNT (1.46 eV) from TS2 to FS. The whole reaction from IS to FS is exothermic by 2.29 eV for N-CNT and 2.58 eV for  $Co_4@N-CNT$  (Figure 6). The above DFT analyses thus suggest that  $Co_4@N-CNT$  can activate both  $H_2$  and nitro group of **1a** more easily than N-CNT, which will evidently contribute a lot for the hydrogenation of **1a**. Moreover, the rate-determining step for transformation of **1a** into **10** is  $H_2$  dissociation with energy barrier of 2.70 eV on  $Co_4@N-CNT$  and 3.54 eV on N-CNT catalyst, respectively.

## Conclusion

In summary,  $Co@CN_{900}/H_2$  was developed as a novel, green, mild, and efficient catalytic system for a wide variety of benzimidazole syntheses by hydrogenative coupling of 2-nitroaniline or 1,2-dinitrobenzene substrates with aldehydes. In addition, robust and recyclable  $Co@CN_{900}$ , which is magnetic in nature, proved a promising catalyst for the current methodology for benzimidazole synthesis. Both the mechanism and the kinetics of the hydrogenative coupling were systematically demonstrated by experimental and theoretical investigations. This research thus extends sustainable applications of the encapsulated transition metal catalysts in thermally induced organic transformations.

## Experimental Section

### Preparation of catalysts

**Co@NC<sub>900</sub>**:  $Co@NC_{900}$  was prepared from a mixture of P123, cobalt acetate tetrahydrate [ $Co(CH_3COO)_2 \cdot 4H_2O$ ] and melamine based on literature method with slight modifications.<sup>[73]</sup> In brief, melamine (2.25 g), P123 (1.5 g) and cobalt acetate tetrahydrate (1.0 g) were dissolved in an ultrapure water (80 mL). The resulting mixture was stirred at room temperature for 2 h, and further stirred for 0.5 h at 80 °C. The solvent was then slowly removed by vacuum-rotary evaporation at 80 °C. The obtained powder was transferred into an alundum boat and heated at 180 °C for 2 h, 240 °C for 2 h and 900 °C for 1 h, respectively, with a heating rate of 2 °C min<sup>-1</sup> under nitrogen atmosphere. The obtained black sample was further leached in HCl (1.0 M) for 12 h at 80 °C, thoroughly washed with deionized water and dried under vacuum to give  $Co@NC_{900}$  (about 700 mg).

**Co@NC<sub>700</sub> and Co@NC<sub>800</sub>**:  $Co@NC_{700}$  and  $Co@NC_{800}$  were prepared following the above synthetic procedure with the final calcination temperature of 700 and 800 °C, respectively.

**NC<sub>900</sub>**:  $NC_{900}$  was synthesized with similar synthetic procedure of  $Co@NC_{900}$  without addition of  $Co(CH_3COO)_2 \cdot 4H_2O$ .

### Synthesis of benzimidazole **4a**

The hydrogenative coupling was carried out in a Teflon-lined stainless-steel autoclave (25 mL) with a magnetic stirrer.  $Co@NC_{900}$  (20 mg), **1a** (0.2 mmol), **3a** (0.4 mmol) and ethyl acetate (4 mL) were successively added into the reactor.  $H_2$  was slowly purged into the autoclave to replace the air inside the reactor for three times.  $H_2$  (1.0 MPa) was then slowly loaded into the reactor. The reaction was carried out at ambient temperature for 20 h. After the reaction, the mixture in the reactor was then examined by Gas Chromatography (GC).

## Acknowledgements

We acknowledge the financial support from National Natural Science Foundation of China (U1810111, 22075104), Natural Science Foundation of Guangdong Province, China (2018B030311010), and Youth Science and Technology Innovation Talent of Guangdong TeZhi Plan (2019TQ05L111).

## Conflict of Interest

The authors declare no conflict of interest.

**Keywords:** cobalt · heterogeneous catalysis · hydrogenation · kinetics · reaction mechanisms.

- [1] J. Deng, D. Deng, X. Bao, *Adv. Mater.* **2017**, *29*, 1606967.
- [2] W. Xia, J. Tang, J. Li, S. Zhang, K. C. W. Wu, J. He, Y. Yamauchi, *Angew. Chem. Int. Ed.* **2019**, *58*, 13354–13359; *Angew. Chem.* **2019**, *131*, 13488–13493.
- [3] J. Wang, G. Han, L. Wang, L. Du, G. Chen, Y. Gao, Y. Ma, C. Du, X. Cheng, P. Zuo, G. Yin, *Small* **2018**, *14*, 1704282.
- [4] H. Tang, S. Cai, S. Xie, Z. Wang, Y. Tong, M. Pan, X. Lu, *Adv. Sci.* **2016**, *3*, 1500265.
- [5] H. Tan, J. Tang, J. Henzie, Y. Li, X. Xu, T. Chen, Z. Wang, J. Wang, Y. Ide, Y. Bando, Y. Yamauchi, *ACS Nano* **2018**, *12*, 5674–5683.
- [6] Z. Liang, X. Fan, H. Lei, J. Qi, Y. Li, J. Gao, M. Huo, H. Yuan, W. Zhang, H. Lin, H. Zheng, R. Cao, *Angew. Chem. Int. Ed.* **2018**, *57*, 13187–13191; *Angew. Chem.* **2018**, *130*, 13371–13375.
- [7] X. Cui, P. Ren, D. Deng, J. Deng, X. Bao, *Energy Environ. Sci.* **2016**, *9*, 123–129.
- [8] D. Lyu, Y. Du, S. Huang, B. Y. Mollamahale, X. Zhang, S. W. Hasan, F. Yu, S. Wang, Z. Q. Tian, P. K. Shen, *ACS Appl. Mater. Interfaces* **2019**, *11*, 39809–39819.
- [9] J. Li, Y. Kang, D. Liu, Z. Lei, P. Liu, *ACS Appl. Mater. Interfaces* **2020**, *12*, 5717–5729.
- [10] H. B. Yang, S. F. Hung, S. Liu, K. Yuan, S. Miao, L. Zhang, X. Huang, H. Y. Wang, W. Cai, R. Chen, J. Gao, X. Yang, W. Chen, Y. Huang, H. M. Chen, C. M. Li, T. Zhang, B. Liu, *Nat. Energy* **2018**, *3*, 140–147.
- [11] H. Zhang, T. Wang, J. Wang, H. Liu, T. D. Dao, M. Li, G. Liu, X. Meng, K. Chang, L. Shi, T. Nagao, J. Ye, *Adv. Mater.* **2016**, *28*, 3703–3710.
- [12] J. Wu, R. M. Yadav, M. Liu, P. P. Sharma, C. S. Tiwary, L. Ma, X. Zou, X. D. Zhou, B. I. Yakobson, J. Lou, P. M. Ajayan, *ACS Nano* **2015**, *9*, 5364–5371.
- [13] Y. Hou, S. Cui, Z. Wen, X. Guo, X. Feng, J. Chen, *Small* **2015**, *11*, 5940–5948.
- [14] J. L. Fiorio, R. V. Goncalves, E. Teixeira-Neto, M. A. Ortuño, N. López, L. M. Rossi, *ACS Catal.* **2018**, *8*, 3516–3524.
- [15] W. Li, J. Artz, C. Broicher, K. Junge, H. Hartmann, A. Besmehn, R. Palkovits, M. Beller, *Catal. Sci. Technol.* **2019**, *9*, 157–162.
- [16] R. L. Oliveira, M. C. Ben Ghorbel, S. Praetz, D. Meiling, C. Schlesiger, R. Schomäcker, A. Thomas, *ACS Sustainable Chem. Eng.* **2020**, *8*, 11171–11182.

- [17] R. L. Oliveira, J. Kerstien, R. Schomäcker, A. Thomas, *Catal. Sci. Technol.* **2020**, *10*, 1385–1394.
- [18] R. V. Jagadeesh, K. Natte, H. Junge, M. Beller, *ACS Catal.* **2015**, *5*, 1526–1529.
- [19] L. Hu, R. Zhang, L. Wei, F. Zhang, Q. Chen, *Nanoscale* **2015**, *7*, 450–454.
- [20] X. Li, C. Zeng, J. Jiang, L. Ai, *J. Mater. Chem.* **2016**, *4*, 7476–7482.
- [21] H. Huang, X. Wang, Y. Sheng, C. Chen, X. Zou, X. Shang, X. Lu, *RSC Adv.* **2018**, *8*, 8898–8909.
- [22] D. Xu, H. Zhao, Z. Dong, J. Ma, *ChemCatChem* **2019**, *11*, 5475–5486.
- [23] T. Ni, S. Zhang, F. Cao, Y. Ma, *Inorg. Chem. Front.* **2017**, *4*, 2005–2011.
- [24] L. Liu, F. Gao, P. Concepción, A. Corma, *J. Catal.* **2017**, *350*, 218–225.
- [25] D. Formenti, C. Topf, K. Junge, F. Ragaini, M. Beller, *Catal. Sci. Technol.* **2016**, *6*, 4473–4477.
- [26] L. Liu, P. Concepción, A. Corma, *J. Catal.* **2016**, *340*, 1–9.
- [27] D. Formenti, F. Ferretti, C. Topf, A. E. Surkus, M. M. Pohl, J. Radnik, M. Schneider, K. Junge, M. Beller, F. Ragaini, *J. Catal.* **2017**, *351*, 79–89.
- [28] X. Sun, A. I. Olivios-Suarez, L. Oar-Arteta, E. Rozhko, D. Osadchii, A. Bavykina, F. Kapteijn, J. Gascon, *ChemCatChem* **2017**, *9*, 1854–1862.
- [29] R. Gao, L. Pan, Z. Li, X. Zhang, L. Wang, J. J. Zou, *Chin. J. Catal.* **2018**, *39*, 664–672.
- [30] D. Formenti, F. Ferretti, F. K. Scharnagl, M. Beller, *Chem. Rev.* **2018**, *119*, 2611–2680.
- [31] J. Li, G. Liu, X. Long, G. Gao, J. Wu, F. Li, *J. Catal.* **2017**, *355*, 53–62.
- [32] W. Gong, Y. Lin, C. Chen, M. Al-Mamun, H. S. Lu, G. Wang, H. Zhang, H. Zhao, *Adv. Mater.* **2019**, *31*, 1808341.
- [33] H. Su, K. X. Zhang, B. Zhang, H. H. Wang, Q. Y. Yu, X. H. Li, M. Antonietti, J. S. Chen, *J. Am. Chem. Soc.* **2017**, *139*, 811–818.
- [34] X. Lin, Z. Nie, L. Zhang, S. Mei, Y. Chen, B. Zhang, R. Zhu, Z. Liu, *Green Chem.* **2017**, *19*, 2164–2173.
- [35] C. Liang, X. Li, D. Su, Q. Ma, J. Mao, Z. Chen, Y. Wang, J. Yao, H. Li, *Mol. Catal.* **2018**, *453*, 121–131.
- [36] T. Fu, M. Wang, W. Cai, Y. Cui, F. Gao, L. Peng, W. Chen, W. Ding, *ACS Catal.* **2014**, *4*, 2536–2543.
- [37] D. Deng, L. Yu, X. Chen, G. Wang, L. Jin, X. Pan, J. Deng, G. Sun, X. Bao, *Angew. Chem. Int. Ed.* **2013**, *52*, 371–375; *Angew. Chem.* **2013**, *125*, 389–393.
- [38] W. Zhou, J. Zhou, Y. Zhou, J. Lu, K. Zhou, L. Yang, Z. Tang, L. Li, S. Chen, *Chem. Mater.* **2015**, *27*, 2026–2032.
- [39] A. A. R. El, H. Y. Aboul-Enein, *Mini-Rev. Med. Chem.*, **2013**, *13*, 399–407.
- [40] B. Narasimhan, D. Sharma, P. Kumar, *Med. Chem. Res.* **2012**, *21*, 269–283.
- [41] P. S. Hameed, A. Raichurkar, P. Madhavapeddi, S. Menasinakai, S. Sharma, P. Kaur, R. Nandishaiah, V. Panduga, J. Reddy, V. K. Sambandamurthy, D. Sriram, *ACS Med. Chem. Lett.* **2014**, *5*, 820–825.
- [42] B. Fang, C. H. Zhou, X. C. Rao, *Eur. J. Med. Chem.* **2010**, *45*, 4388–4398.
- [43] M. M. Sirim, V. S. Krishna, D. Sriram, O. U. Tan, *Eur. J. Med. Chem.* **2020**, *188*, 112010.
- [44] S. N. A. Bukhari, G. Lauro, I. Jantan, C. F. Chee, M. W. Amjad, G. Bifulco, H. Sher, I. Abdullah, N. A. Rahman, *Future Med. Chem.* **2016**, *8*, 1953–1967.
- [45] L. M. Dudd, E. Venardou, E. Garcia-Verdugo, P. Licence, A. J. Blake, C. Wilson, M. Poliakov, *Green Chem.* **2003**, *5*, 187–192.
- [46] J. C. Lewis, J. Y. Wu, R. G. Bergman, J. A. Ellman, *Angew. Chem. Int. Ed.* **2006**, *45*, 1589–1591; *Angew. Chem.* **2006**, *118*, 1619–1621.
- [47] C. A. Wang, Y. F. Han, K. Nie, Y. W. Li, *Mater. Chem. Front.* **2019**, *3*, 1909–1917.
- [48] X. Sang, X. Hu, R. Tao, Y. Zhang, H. Zhu, D. Wang, *ChemPlusChem* **2020**, *85*, 123–129.
- [49] A. Kumar, R. A. Maurya, P. Ahmad, *J. Comb. Chem.* **2009**, *11*, 198–201.
- [50] K. Bahrami, M. M. Khodaei, F. Naali, *J. Org. Chem.* **2008**, *73*, 6835–6837.
- [51] X. Diao, Y. Wang, Y. Jiang, D. Ma, *J. Org. Chem.* **2009**, *74*, 7974–7977.
- [52] Y. Shiraiishi, Y. Sugano, S. Tanaka, T. Hirai, *Angew. Chem. Int. Ed.* **2010**, *49*, 1656–1660; *Angew. Chem.* **2010**, *122*, 1700–1704.
- [53] L. Hao, Y. Zhao, B. Yu, H. Zhang, H. Xu, Z. Liu, *Green Chem.* **2014**, *16*, 3039–3044.
- [54] J. C. Lewis, A. M. Berman, R. G. Bergman, J. A. Ellman, *J. Am. Chem.*, **2008**, *130*, 2493–2500.
- [55] D. Yang, D. Fokas, J. Li, L. Yu, C. M. Baldino, *Synthesis* **2005**, *2005*, 47–56.
- [56] P. L. Beaulieu, B. Hache, E. V. Moos, *Synthesis* **2003**, *2003*, 1683–1692.
- [57] B. Krzyzinska, M. Glazek, A. Maczynska, *Acta Agrobot.* **2005**, *58*, 37–42.
- [58] T. H. Thomas, *Ann. Appl. Biol.* **1974**, *76*, 237–241.
- [59] F. G. Sánchez, A. N. Díaz, A. G. Pareja, *J. Liq. Chromatogr. Relat. Technol.* **1995**, *18*, 2543–2558.
- [60] S. Liu, Z. Wang, S. Zhou, F. Yu, M. Yu, C. Y. Chiang, W. Zhou, J. Zhao, J. Qiu, *Adv. Mater.* **2017**, *29*, 1700874.
- [61] J. Kang, H. Zhang, X. Duan, H. Sun, X. Tan, S. Liu, S. Wang, *Chem. Eng. J.* **2019**, *362*, 251–261.
- [62] Z. Chen, R. Wu, Y. Liu, Y. Ha, Y. Guo, D. Sun, M. Liu, F. Fang, *Adv. Mater.* **2018**, *30*, 1802011.
- [63] Q. Lin, X. Bu, A. Kong, C. Mao, F. Bu, P. Feng, *Adv. Mater.* **2015**, *27*, 3431–3436.
- [64] Y. Liu, H. Jiang, Y. Zhu, X. Yang, C. Li, *J. Mater. Chem.* **2016**, *4*, 1694–1701.
- [65] Y. Zhang, P. Cao, H. Y. Zhang, G. Yin, J. Zhao, *Catal. Commun.* **2019**, *129*, 105747.
- [66] A. Primo, F. Neatu, M. Florea, V. Parvulescu, H. Garcia, *Nat. Commun.* **2014**, *5*, 5291.
- [67] D. S. Wang, Q. A. Chen, S. M. Lu, Y. G. Zhou, *Chem. Rev.* **2012**, *112*, 2557–2590.
- [68] X. Chen, Q. Shen, Z. Li, W. Wan, J. Chen, J. Zhang, *ACS Appl. Mater. Interfaces* **2020**, *12*, 654–666.
- [69] H. Namli, O. Turhan, *Vib. Spectrosc.* **2007**, *43*, 274–283.
- [70] J. Zeng, W. Zhang, Y. Yang, D. Li, X. Yu, Q. Gao, *ACS Appl. Mater. Interfaces* **2019**, *11*, 33074–33081.
- [71] M. Xing, L. Guo, Z. Hao, *Catal. Lett.* **2018**, *148*, 2117–2126.
- [72] P. Bechthold, M. E. Pronso, C. Pistonesi, *Appl. Surf. Sci.* **2015**, *347*, 291–298.
- [73] W. Yang, L. Chen, X. Liu, J. Jia, S. Guo, *Nanoscale* **2017**, *9*, 1738–1744.

Manuscript received: October 4, 2020  
Revised manuscript received: November 1, 2020  
Version of record online: ■■■, ■■■■

## FULL PAPERS

**Seek and you confided:** Co nanoparticles encapsulated in N-doped carbon nanotubes can efficiently catalyze hydrogenative coupling for the synthesis of benzimidazoles. The robust catalyst can be easily recovered by an external magnetic field and readily recycled. Potential industrial application of the earth-abundant metal catalysts is thus demonstrated for green synthesis of heterocyclic compounds.



C. Lin, W. Wan, X. Wei, Prof. J. Chen\*

1 – 13

**H<sub>2</sub> Activation with Co Nanoparticles Encapsulated in N-Doped Carbon Nanotubes for Green Synthesis of Benzimidazoles**

